Check for updates

View Article Online
View Journal

Nanoscale

Accepted Manuscript

This article can be cited before page numbers have been issued, to do this please use: Z. Ismail, Y. Li, J. Lei, S. Man, K. T. Kubra, Y. Xiong, C. Zhang and J. Low, *Nanoscale*, 2026, DOI: 10.1039/D5NR05061H.

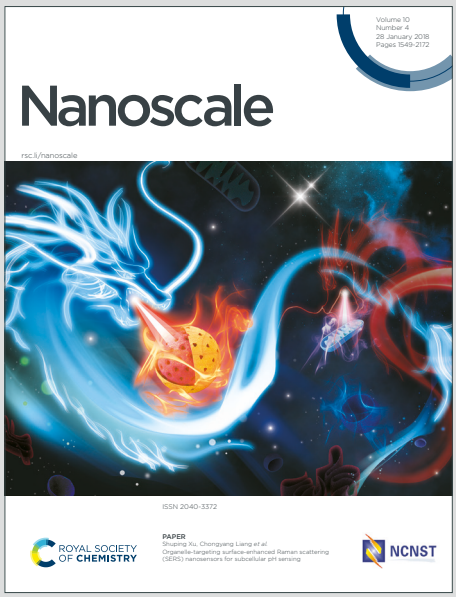

This is an Accepted Manuscript, which has been through the Royal Society of Chemistry peer review process and has been accepted for publication.

Accepted Manuscripts are published online shortly after acceptance, before technical editing, formatting and proof reading. Using this free service, authors can make their results available to the community, in citable form, before we publish the edited article. We will replace this Accepted Manuscript with the edited and formatted Advance Article as soon as it is available.

You can find more information about Accepted Manuscripts in the Information for Authors.

Please note that technical editing may introduce minor changes to the text and/or graphics, which may alter content. The journal's standard Terms & Conditions and the Ethical guidelines still apply. In no event shall the Royal Society of Chemistry be held responsible for any errors or omissions in this Accepted Manuscript or any consequences arising from the use of any information it contains.

ROYAL SOCIETY OF CHEMISTRY

rsc.li/nanoscale

Please do not adjust margins

View Article Online
DOI: 10.1039/D5NR05061H

ARTICLE

Design of 2D/1D $Bi_2MoO_6/Bi_{19}S_{27}Br_3$ direct Z-scheme heterojunction with built-in internal electric field for enhanced CO_2 photocatalytic reduction performance

Zakaria Ismail[a], You Li[a], Jian Lei[b], Saira Man[a], Khadija Tul Kubra[c], Chao Zhang*[b], Jingxiang Low[d], Yujie Xiong*[a,b]

Received 00th January 20xx,
Accepted 00th January 20xx

DOI: 10.1039/x0xx00000x

Bi-based heterojunctions have garnered extensive attention in photocatalytic carbon dioxide (CO_2) reduction due to their efficient charge separation and strong redox ability. The built-in internal electric field (IEF) at the interface of the direct Z-scheme heterojunction interface serves as the driving force for charge transfer, however, suboptimal interfacial contact often restricts the carrier migration efficiency. Herein, we meticulously tune the contact interface over a Bi-based heterojunction by modulating the morphologies of the semiconductor components. Specifically, we synthesize a 2D/1D $Bi_2MoO_6/Bi_{19}S_{27}Br_3$ (BMO/BSBr) direct Z-scheme heterostructure by embedding 1D BSBr nanorods onto 2D BMO nanosheets. Such a contact interface can optimize the photogenerated charge carrier migration across the BMO and BSBr, thereby significantly promoting their separation. As a result, the photocatalytic CO_2 conversion performance of the optimized BMO/BSBr reaches 34.4 μmol g^{-1} h^{-1}, exceeding those of BMO and BSBr by 4.5 and 19.8-folds, respectively. The mechanisms underlay this enhanced photocatalytic performance are revealed via in situ diffuse reflectance infrared Fourier transform spectroscopy (DRIFTS), X-ray photoelectron spectroscopy and radicals trapping tests, showing that the internal electric field along with the fine-tuned contact interface hold the key for momentously boosting the photogenerated charge carrier utilization efficiency. This study provides a novel design strategy for constructing high-performance photocatalysts via chemical bonding interfacial, offering efficient charge transfer and high catalytic activity.

Introduction

The evolution of photocatalysis, which relies solely on incident solar energy for driving chemical reactions, provides a potential solution for resolving energy crises and environmental issues.[1-4] Amidst the development of photocatalysis, photocatalytic CO_2 conversion has been attracted widespread attention as it can simultaneously mitigate CO_2 concentration in the atmosphere and produce valuable chemicals.[5-7] Throughout recent decades, vast arrays of photocatalytic semiconductor materials have been engineered for use in the photocatalytic CO_2 reduction.[7-12] However, due to intense electron-hole pair recombination, insufficient catalytic active centers, and the high bond energy barrier for dissociation of the C═O bond (750 kJ mol^{-1}), achieving efficient photocatalytic CO_2 reduction remains challenging in practical production[13, 14]. Therefore, the current efficiency of photocatalytic CO_2 reduction falls far below the threshold required for industrial standards.[15-17]

Focusing on optimizing the three critical steps in the photocatalytic CO_2 reduction process, a central challenge lies in engineering photocatalytic materials with superior light harvesting, sufficient catalytic active centers, and highly efficient electron-hole pair separation. Countless strategies have been pursued to address these limitations, such as constructing vacancy engineering,[18-20] ultra-thin structures,[21, 22] doping elements,[23, 24] and fabricating heterojunctions.[25, 26] The construction of heterojunction has been extensively studied in photocatalytic CO_2 reduction.[27-29] The choice of suitable semiconductors for integrating specific heterojunction types, such as step-scheme (S-scheme)[30-32] and direct Z-scheme[33-36] configurations, is critical. The formation of strong bonds at the hetero-interface, serves a crucial role in enhancing interfacial carrier migration and optimizing performance. Consequently, creating interfacial interatomic bonds in heterostructures is considered a key strategy to maximize the efficiency of photocatalytic CO_2 reduction.[37-43]

The interfacial interatomic bonds can dictate the interfacial charge distribution and minimize the interfacial conductivity in

[a.] School of Chemistry and Materials Science, Hefei National Research Center for Physical Sciences at the Microscale, Key Laboratory of Precision and Intelligent Chemistry, University of Science and Technology of China, Hefei, Anhui 230026, China
E-mail: yjxiong@ustc.edu.cn
E-mail: zc1992@ustc.edu.cn
[b.] Anhui Engineering Research Center of Carbon Neutrality, The Key Laboratory of Functional Molecular Solids, Ministry of Education, Anhui Laboratory of Molecular-Based Materials, College of Chemistry and Materials Science, Anhui Normal University, Wuhu, Anhui 241002, China
[c.] National Synchrotron Radiation Laboratory, School of Nuclear Science and Technology, The Experimental Center of Engineering and Material Sciences, University of Science and Technology of China, Hefei, Anhui 230026 China.
[d.] School of Physical Science and Technology, School of Materials Science and Engineering, Tiangong University, Tianjin 300387, China
† Footnotes relating to the title and/or authors should appear here.
Supplementary Information available: [details of any supplementary information available should be included here]. See DOI: 10.1039/x0xx00000x

Open Access Article. Published on 02 March 2026. Downloaded on 3/3/2026 11:48:45 PM.
This article is licensed under a Creative Commons Attribution-NonCommercial 3.0 Unported Licence.
Nanoscale Accepted Manuscript

Open Access Article. Published on 02 March 2026. Downloaded on 3/3/2026 11:48:45 PM. This article is licensed under a Creative Commons Attribution-NonCommercial 3.0 Unported Licence.

the contact resistance region, which will substantially improve the yield of transmission and separation of photogenerated charges and enhance the photoinduced activity.[44-47] A diverse range of semiconductor materials has been designed for use in photocatalytic CO_2 reduction applications. Among them, Bismuth-based (Bi-based) photocatalytic materials, such as Bi_2MoO_6 (BMO),[48-50] $BiVO_4$,[51-53] and Bi_2WO_6,[54-56] have attracted extensive attention recently due to their controllable synthesis, unique crystal structures, and eco-friendliness.

BMO, as a conventional Bi-based semiconductors oxide, is reckoned as an auspicious photocatalytic material as a result of its durable, stable physicochemical and proper wide band gap (~2.7 eV).[57-59] However, there are some setbacks to the improvement of pure BMO as a photocatalyst due to the excessive electron-hole recombination rate.[60-62] Various procedures, including controlling the morphology and integrating two-dimensional (2D) nanosheets (NSs) BMO with other materials to construct a remarkable heterojunction, have been implemented to enhance the efficient separation of charges and improve the CO_2 adsorption capacity for the photoreduction of CO_2.[62, 63]

Additionally, among the Bi-based V–VI–VII group narrow bandgap semiconductors, $Bi_{19}S_{27}Br_3$ (BSBr) stands out due to its superior light absorption capability, remarkable electrical conductivity, and an appropriately positioned negative CB band. These characteristics make BSBr a promising candidate for photocatalytic CO_2 reduction applications.[64-68] One-dimensional (1D) BSBr nanorods (NRs) have been extensively combined with diverse materials, such as In_2O_3, g-C_3N_4, and $SnIn_4S_8$, to build heterostructure composites with interfacial bonds, promoting the photoreduction of CO_2 into value-added products.[69-71] Based on these observations, the tight interatomic contact at the interface region of the heterojunction cannot be overlooked. Thus, the synergistic coupling effects between 2D/1D with formation of interatomic bonds in the interfacial region of heterostructures can facilitate photoinduced charge separation and surface redox reactions to enhanced photocatalytic activity and reaction selectivity of CO_2 Photoreduction.

Here, the strategically construction of a 2D/1D BMO/BSBr direct Z-scheme composite heterojunction structure, formed from 2D BMO nanosheets and 1D BSBr nanowires with built-in internal electric field (IEF) and interfacial interatomic bonds, is anticipated to be an ideal design for achieving highly photocatalytic efficient for CO_2. The presence of IEF facilitates the combination of conduction band (CB) electrons from BMO and valence band (VB) holes from BSBr. Additionally, these strong built-in IEF and interatomic bonds interaction prevent the dissociation of the BMO and BSBr heterojunction during photocatalytic CO_2 reduction process, providing a relatively efficient and stable photocatalytic system. Meanwhile, electrons with high reduction ability from BSBr and holes with high oxidation ability participate in the redox reaction. This study introduces an innovative approach to synergistically regulate 2D/1D direct Z-scheme heterojunctions system through a built-in IEF and interfacial interatomic bonding to achieve efficient CO_2 photocatalytic activity.

Experimental

View Article Online
DOI: 10.1039/D5NR05061H

Materials

Ammonium molybdate tetrahydrate $(NH_4)_6Mo_7O_{24}.4H_2O$), thiourea, bismuth nitrate pentahydrate ($Bi(NO)_3{\cdot}5H_2O$), Ammonia solution, Nafion, ethylene glycol, ethanol and cetyltrimethylammonium bromide (CTAB) were purchased by Shanghai Sinopharm Chemical Reagent Co. Ltd (P. R. China). Deionized (DI) water was used throughout the study. All reactants were of analytical purity and used as received, without further purification.

Preparation of BMO

In a typical synthesis, BMO was prepared via a hydrothermal method. First, 3 mmol of $Bi(NO)_3{\cdot}5H_2O$ was dispersed in 40 mL of DI water under magnetic stirring for 30 min to ensure complete dissolution. Subsequently, 0.214 mmol $NH_4)_6Mo_7O_{24}.4H_2O$ was added to the solution under continuous stirring for an additional 30 min to form a homogeneous precursor mixture. The pH of the solution was then adjusted to neutral (pH = 7) by dropwise addition of ammonium hydroxide (NH_4OH, 28%) under constant stirring. The solution was transferred into a 50 mL Teflon-lined autoclave for thermal treatment at 160 °C for 10 h. The sample was collected by centrifugation and washed several times using DI water. The final product was dried in a vacuum oven at 70 °C for 24 h obtain BMO NSs.

Preparation of X-BMO/BSBr and BSBr

The X-BMO/BSBr composites (where X = 1, 2, 3 and 4 corresponds to 10, 20, 40, and 80 mg of BMO, respectively) were synthesized through a modified solvothermal method. In a typical procedure, the predetermined amount of BMO was first dispersed in 30 mL ethylene glycol under vigorous magnetic stirring for 30 min. Subsequently, 0.46 mmol thiourea, 0.40 mmol CTAB, and 0.02 mmol $Bi(NO)_3{\cdot}5H_2O$ were sequentially added to the suspension. The mixture was maintained under continuous vigorous stirring for 4 h at room temperature to ensure complete precursor homogenization. The solution was then transferred to a 50 mL Teflon-lined autoclave and subjected to thermal treatment at 403 K for 10 h. Subsequently, the products were collected by centrifugation and washed alternately with ethanol and DI water many times. Then, the samples were dried in a vacuum oven at 343 K for 24 h. For comparison, pristine BSBr was synthesized following the identical method without the addition of BMO precursor.

Results and discussion

Characterization and preparation of catalysts

In this work, the 2D/1D BMO/BSBr heterostructure composites were synthesized by mixing the primary precursors under controlled conditions using the solvothermal method, and the construction process is depicted in Figure 1a. The interface interactions between 1D BSBr NRs and 2D BMO NSs in BMO/BSBr heterostructure were further investigated. The x-ray diffraction (XRD) patterns of pure BMO, BSBr, and the

Nanoscale Accepted Manuscript

Please do not adjust margins

View Article Online
DOI: 10.1039/D5NR05061H

Open Access Article. Published on 02 March 2026. Downloaded on 3/3/2026 11:48:45 PM.
This article is licensed under a Creative Commons Attribution-NonCommercial 3.0 Unported Licence.

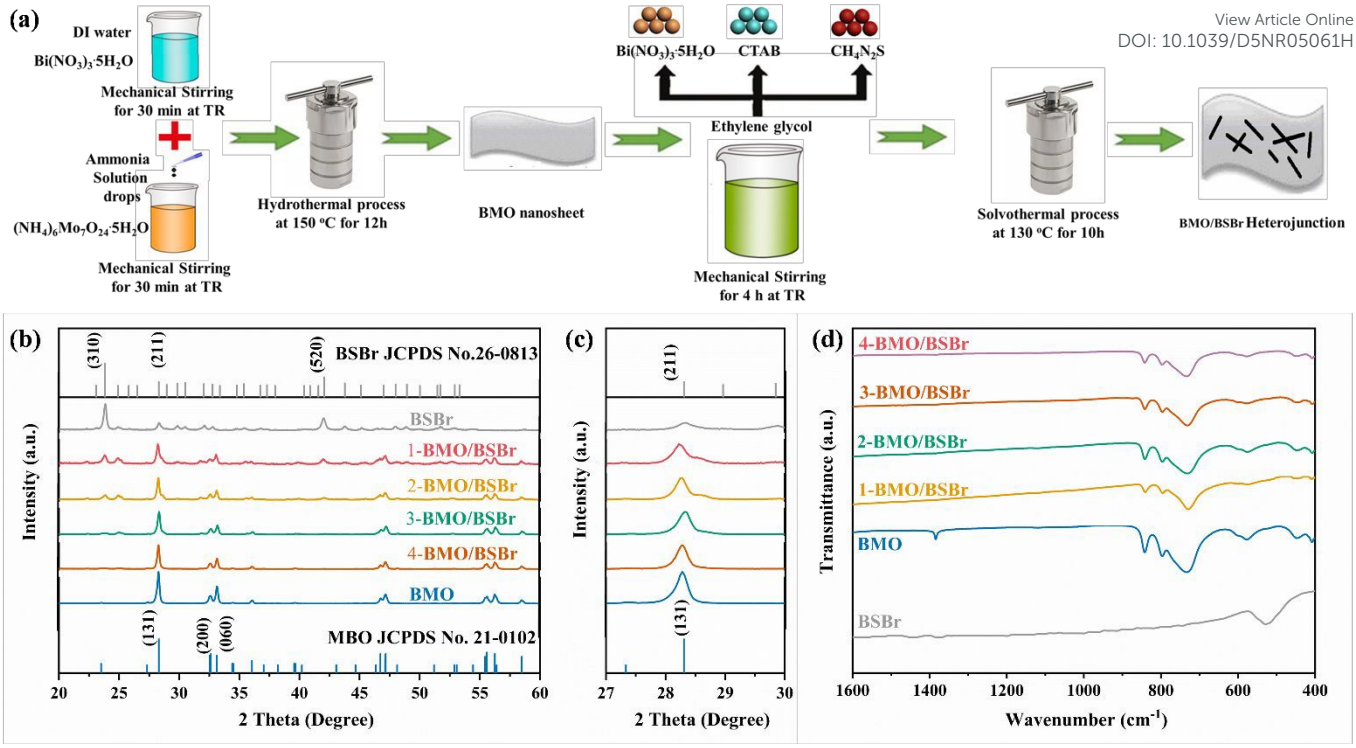

Figure 1. (a) Preparation process of BMO/BSBr heterojunctions. (b), (c) XRD patterns, and (d) FTIR spectra of BMO/BSBr Heterojunctions.

synthesized BMO/BSBr composites are demonstrated in Figure 1b. The diffraction peaks of the synthesized BMO at 2θ values of 28.3°, 32.5°, 33.1° etc., can be assigned to the crystal planes (131), (200), (060) etc., respectively, matching with orthorhombic crystal structure of BMO (JCPDS No. 21-0102).[72] Moreover, the prepared BSBr demonstrates the XRD peaks attributed to the hexagonal BSBr (JCPDS Card No. 26-0813).[68] In addition, all the synthesized BMO/BSBr heterostructures demonstrate the XRD peaks attributed to the BMO and BSBr. However, as the concentration of BMO increased the diffraction peak corresponding to the (131) crystallographic plane of BMO exhibited a significant increase in sharpness (Figure 1c). That suggesting successful coupling of these two semiconductors.

Fourier transform infrared (FTIR) spectra (Figure 1d) of BMO, BSBr, and BMO/BSBr were also obtained to shed some light on their surface functional groups. The primary absorption bands of BMO, observed in the range of 400–950 cm^{-1}, are associated with stretching vibrations of Bi–O and Mo–O bonds, as well as Mo–O–Mo bridging stretching modes.[73, 74] Additionally, the peaks at 1380 cm^{-1} are attributed to O–H stretching vibration attributed to the surface adsorbed H_2O.[75] Moreover, BSBr spectrum showed weak peak at 500 cm^{-1}, belonging to the vibrational state of the Bi–O bonds.[49, 70, 76] Notably, after coupling BMO with BSBr, the FTIR spectrum of BMO/BSBr exhibits negligible changes, suggesting that the presence of the BMO does not alter the surface functional groups on the BSBr.

X-ray photoelectron spectroscopy (XPS) was assessed for gaining insights into the compositional structures and surface elemental and chemical valence of the prepared samples. The high-resolution Bi 4f, S 2p, Mo 3d, Br 3d, and O 1s XPS spectra of BMO, BSBr, and 2-BMO/BSBr were shown in Figure 2. As shown in Figure S1, Bi, Mo, S, Br, and O elements can be observed in the XPS survey spectrum of the 2-BMO/BSBr composite, confirming coupling of BMO with BSBr. For the high-resolution Bi 4f and S 2p XPS spectra (Figure 2a), the deconvoluted peaks of the BMO and BSBr samples reveal two distinct binding energy peaks corresponding to Bi-$4f_{5/2}$ and Bi-$4f_{7/2}$ doublet, confirming the presence of Bi^{3+} in both materials. In the 2-BMO/BSBr heterojunction the observed signals of Bi 4f can be assigned to Bi^{3+} ions originating from both the BMO[77-79] and BSBr[72, 80, 81] components. Furthermore, all Bi 4f peaks in the heterojunction exhibit a clear shift toward lower binding energy compared to the individual components, a direct result of electronic interaction at the heterojunction interface. Meanwhile, the deconvoluted peaks of S 2p for both bare semiconductors and the 2-BMO/BSBr composite (Figure 2a) corresponding to S-$2p_{1/2}$ and S-$2p_{3/2}$ states, confirming the presence of S^{2-} in all materials.[82] As a result of heterojunction formation, these two S 2p peaks shift to a lower binding energy. In Figure 2b, the BMO sample reveals two distinct strong binding energy peaks corresponding to Mo $3d_{7/2}$ and Mo $3d_{5/2}$, respectively. For the 2-BMO/BSBr sample, these peaks are still present but shift slightly to a lower binding energy, confirming the presence of Mo^{6+} in both materials. Additionally, a new peak at 224.98 eV appears in the composite, indicating the formation of the Bi-S bonding between BMO and BSBr heterojunction interface.[72, 76] Furthermore, two weak peaks located at 234.04 and 231.07 eV indicate the presence of Mo^{5+}.[83] In Figure 2c,

Nanoscale Accepted Manuscript

Please do not adjust margins

View Article Online
DOI: 10.1039/D6NR00161H

Open Access Article. Published on 02 March 2026. Downloaded on 3/3/2026 11:48:45 PM.
This article is licensed under a Creative Commons Attribution-NonCommercial 3.0 Unported Licence.

Nanoscale Accepted Manuscript

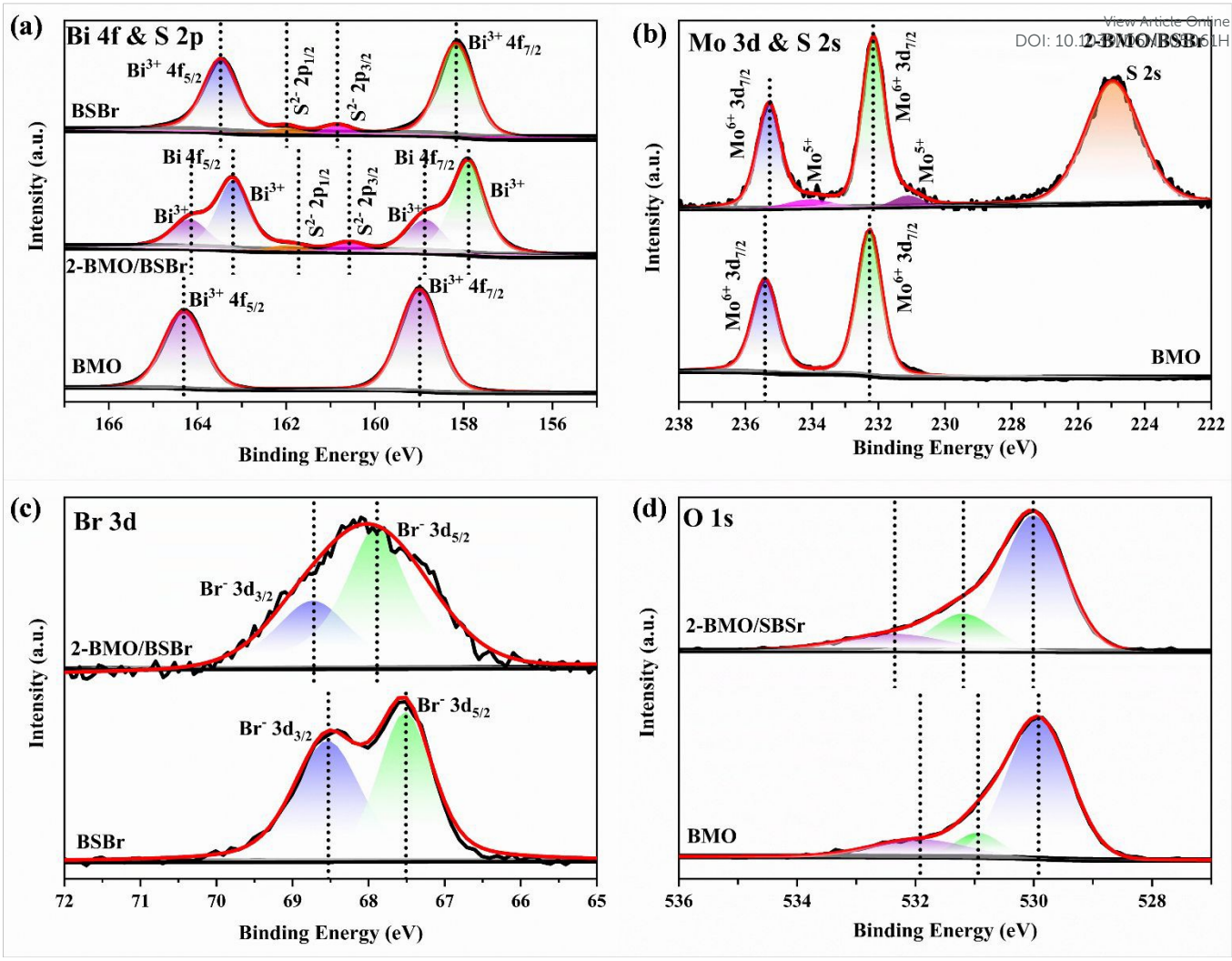

Figure 2. (a-d) XPS spectra of Bi, S, Mo, Br, and O in BMO, BSBr, and 2-BMO/BSBr.

BSBr and 2-BMO/BSBr spectra reveal two deconvoluted peaks corresponding to Br $3d_{3/2}$ and Br $3d_{5/2}$, confirming the presence of Br^- in the samples.[84, 85] In the 2-BMO/BSBr heterojunction, these peaks shift to a higher binding energy compared to bare BSBr. The deconvoluted O 1s XPS spectra of BMO (Figure 2d) exhibit three distinct peaks, which can be assigned to Mo–O, Bi–O, and surface adsorption oxygen, respectively.[86, 87] These same peaks are also observed in the 2-BMO/BSBr heterojunction, but with a shift to higher binding energy. This shift confirms affirming the loading of BMO on the BSBr. Notably, the XPS results reveal a negative shift in the Bi 4f and S 2s peaks, while the Br 3d and O 1s peaks exhibited a positive shift over the 2-BMO/BSBr compared to its single component counterparts,[85] suggesting charge density redistribution and confirming the presence of strong interatomic chemical bonds interaction.[88]

The scanning electron microscope (SEM) image of BMO (Figure S2a) reveals its nanosheet morphology, whereas BSBr exhibits a nanorod morphology (Figure S2b). Figures S2c–f further illustrates the morphological details of the BMO/BSBr, confirming the effective formation of the heterojunction configuration. Transmission electron microscopy (TEM) images (Figures S3a–c) corroborate these structural features. In addition, energy dispersive spectroscopy (EDS) elemental mapping images confirm the presence of Bi, Mo, O for BMO and Bi, S, and Br in BSBr NRs (Figures S3d-k). The micro-morphology of the synthesized samples was investigated using high-resolution TEM (HRTEM). As shown in Figures 3a–c, lattice fringes of 0.315 and 0.372 nm can be observed on the BMO and BSBr, corresponding to the (313) plane of BMO and (310) plane of BSBr, respectively (see also Figures S4a–b for the corresponding SAED patterns). For the 2-BMO/BSBr composite (Figure 3c), two distinct lattice spacings of 0.314 and 0.375 nm can be identified, matching the (313) plane of BMO NSs and the (310) plane of BSBr NRs, respectively. These findings confirm the strong interfacial interaction between BSBr NRs and the surface of BMO NSs, facilitating the formation of a 2D/1D heterojunction through the synthesized process. The corresponding SAED patterns for 2-BMO/BSBr composite are illustrated in Figure S4c. EDS elemental mappings (Figures 3d–i) confirmed the presence of Bi, Mo, O, S, and Br within the composite materials. Additionally, EDS analysis (Figure S5) reveals these elementals composition in the prepared 2-BMO/BSBr sample, which are consistent with the expected

Please do not adjust margins

View Article Online

Open Access Article. Published on 02 March 2026. Downloaded on 3/3/2026 11:48:45 PM. This article is licensed under a Creative Commons Attribution-NonCommercial 3.0 Unported Licence.

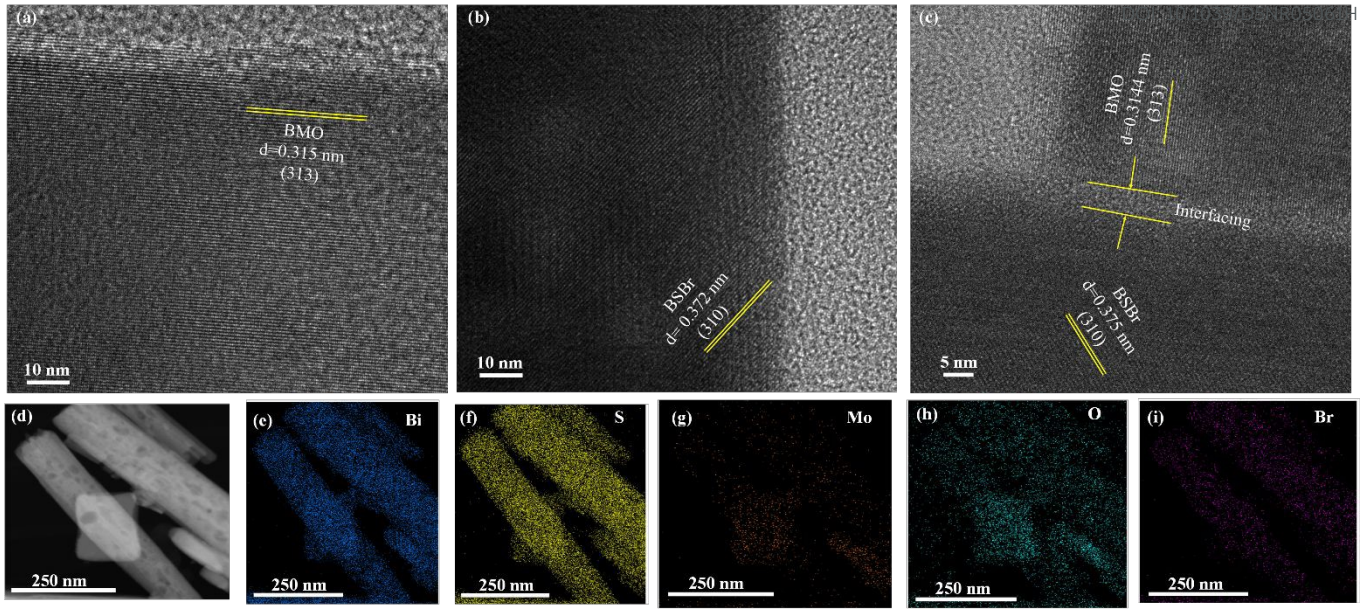

Figure 3. (a-c) HRTEM images of BMO, BSBr, and 2-BMO/BSBr. (d-i) Element mapping of 2-BMO/BSBr sample.

stoichiometric composition**.**

Band structures and surface structures

The optical properties of the synthesized photocatalysts were further investigated using ultraviolet-visible diffuse reflectance spectroscopy (UV-Vis DRS) (Figure 4a). BMO displays a narrow visible light absorption edge at approximately 430 nm, while unmodified BSBr exhibits a broader absorption range and a stronger visible light absorption capacity. Significantly, the BMO/BSBr composites demonstrate a pronounced red shift in absorption edge with increasing BSBr content compared to pure BMO, indicating enhanced visible light absorption. These results highlight the importance of optimizing both the doping ratio and heterostructure design to improve visible light harvesting and consequently enhance photocatalytic performance. Additionally, the Tauc plots are illustrated in Figure 4b based on UV-Vis DRS results, showing the bandgap values of BMO and BSBr to be 2.75 and 1.53 eV, respectively.

To further explore the band structure of the BMO and BSBr, the VB positions of the semiconductors were measured using VB-XPS. Figure 4c depicts the VB-XPS spectra of BMO and BSBr, revealing values of 2.31 and 0.64 eV, respectively. The VB-XPS potential was calculated based on the following equation:[65]

$$E_{VB-NHE} = \varphi + E_{VB-XPS} - 4.44$$

where E_{VB-NHE} is the VB potential vs. NHE and φ= 4.2 eV is the work function. Therefore, the E_{VB-NHE} of BMO and BSBr can be determined to be 2.07 and 0.4 V, respectively. Based on these results, the band structures of BMO and BSBr can be illustrated in Figure 4d. Specifically, the CB and VB band positions of the BMO are more positive than those of the BSBr, laying a foundation for the formation of the heterojunction structure and charges flow pathway.

The surface texture is a critical factor influencing the performance of photocatalytic CO_2 reduction, as it directly determines the CO_2 adsorption capacity **of the** material. As shown in Figure S6, the surface area and pore structure of BMO, BSBr, a nd 2-BMO/BSBr were examined using N_2 adsorption-desorption isotherms via using the Brunauer–Emmett–Teller (BET). All samples exhibited type-IV adsorption-desorption curves with H3-type hysteresis isotherms loops, confirming the presence of a mesoporous structure in the synthesized materials. Furthermore, the BET surface areas of BMO and BSBr were measured to be 19.23 m^2/g and 7.11 m^2/g, respectively. After hybridization, the BET surface area of the 2-BMO/BSBr composite increased significantly to 38.32 m^2/g. This substantial increase in specific surface area for the 2-BMO/BSBr composite confirms the formation of an ideal architecture structure, which reduces the aggregation of 2D BMO NSs and 1D-shaped morphologies of BSBr NRs that typically exhibit fewer mesopores and lower specific surface areas. The enhancement is attributed to the increased surface undulations resulting from the attachment and integration of 1D BSBr NRs.

Charge separation and transfer

The variations in the efficiency of the photogenerated electron-hole separation rate for the synthesized samples were thoroughly evaluated using photoluminescence (PL) spectroscopy. Generally, the separation rate efficiency is inversely proportional to the PL emission intensity, where lower PL intensity typically indicates a lower recombination rate and higher efficiency.[88-90] To assess this, PL spectra were recorded at an excitation wavelength of 325 nm for the samples BMO, BSBr, and 2-BMO/BSBr (Figure 5a). The samples BMO and 2-BMO/BSBr revealed broad emission peaks centered around 450 nm, while the PL spectra of BSBr displayed emission peaks centered at approximately 430 nm. A closer examination showed that 2-BMO/BSBr exhibited notably lower PL emission intensity compared to the bare BMO and BSBr samples.

Nanoscale Accepted Manuscript

Please do not adjust margins

View Article Online
DOI: 10.1039/D5NR05061H

Open Access Article. Published on 02 March 2026. Downloaded on 3/3/2026 11:48:45 PM.
This article is licensed under a Creative Commons Attribution-NonCommercial 3.0 Unported Licence.

Nanoscale Accepted Manuscript

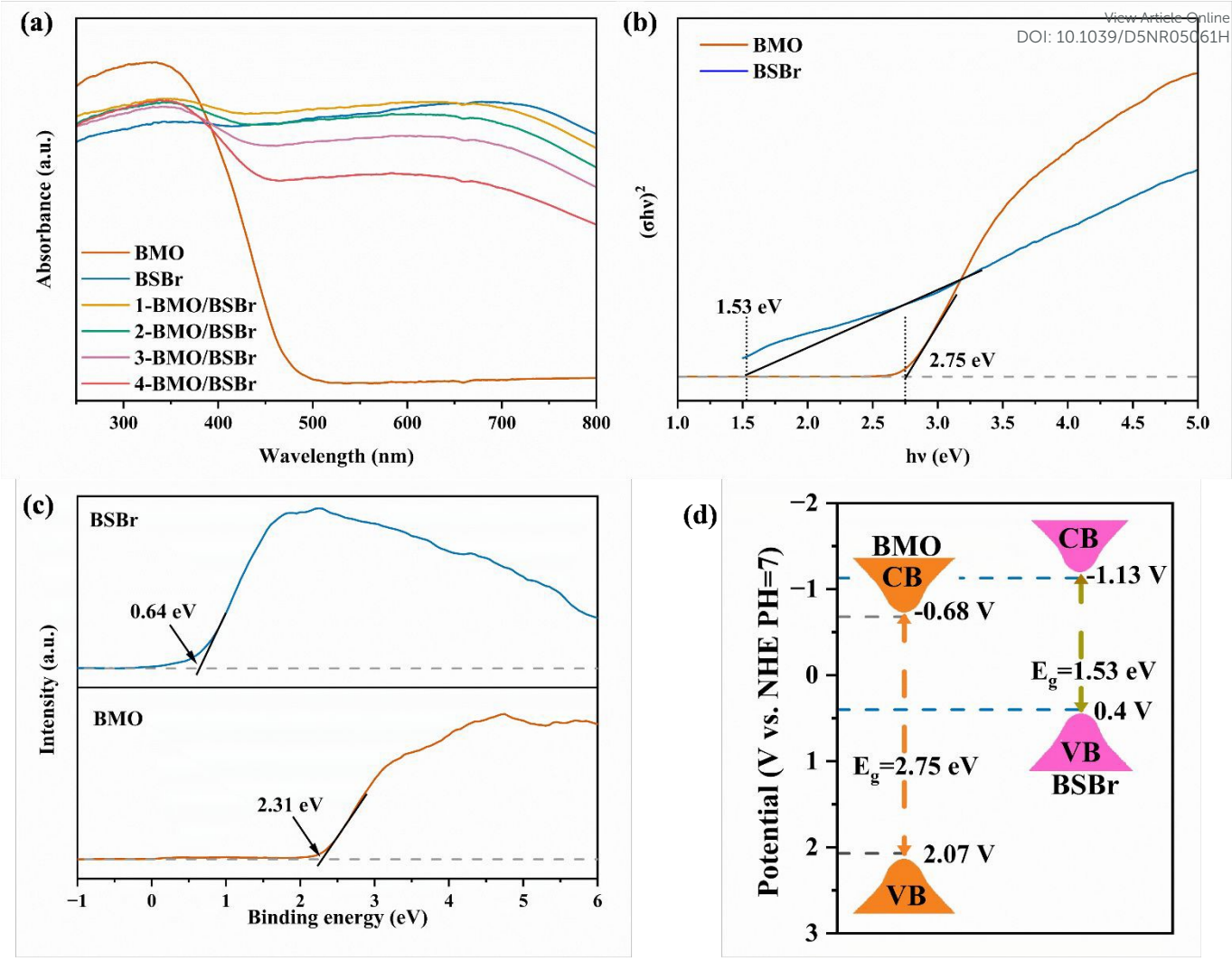

Figure 4. a) UV/Vis DRS spectra of the prepared samples. b) Band gaps for BMO and BSBr samples. c) VB XPS spectra for BMO and BSBr samples. d) The schematic energy level diagrams of BMO and BSBr samples.

Additionally, the emission peak of the composite was broader, further indicating that the recombination of photoinduced charges was effectively suppressed at the interface of the two materials, thereby improving the overall photocatalytic performance.

Transient photoresponse (TPR) and electrochemical impedance spectroscopy (EIS) were used to evaluate the charge transfer and separation efficiency of the synthesized BMO, BSBr, and 2-BMO/BSBr materials. The TPR test conducted under intermittent irradiation with a 20-second interval, is depicted in Figure 4b. The photocurrent densities of BMO, BSBr, and 2-BMO/BSBr exhibited significant fluctuations, rapidly increasing and decreasing when the light illumination was turned on and off, respectively. This behavior reflects their strong photoelectric conversion ability under light irradiation. Notably, the 2-BMO/BSBr composite revealed a substantially higher photocurrent density compared to the pristine BMO and BSBr samples, indicating enhanced separation efficiency of electron-hole pairs within the heterostructure. For pure BSBr, the initial cycles of light illumination and darkness generated a large photocurrent during illumination and a lower photocurrent in the absence of light, followed by the formation of rapid on-and-off spikes. This phenomenon is attributed to the recombination of photoinduced electron-hole pairs at the interface between the electrode and the electrolyte. In contrast, the 2-BMO/BSBr exhibits a distinct behavior when the light source was turned on or off, without the spike behavior observed in BSBr. In addition, the photocurrent density drops smoothly to zero, unlike the changes seen in BSBr. This decay indicates that the 2-BMO/BSBr effectively suppresses the recombination of charge carriers, further confirming its superior charge separation properties.[65, 71] Figure 4c shows the EIS spectra of the synthesized samples. The arc radius of 2-BMO/BSBr is markedly smaller than that of the BMO and BSBr, indicating the significantly reduced interfacial charge carrier transfer resistance on the 2-BMO/BSBr. When considering these findings alongside the PL spectroscopy and EIS results, it can be concluded that the 2-BMO/BSBr heterostructure exhibits superior charge carrier dynamics.

Photocatalytic CO_2 reduction

Please do not adjust margins

View Article Online
DOI: 10.1039/D5NR05061H

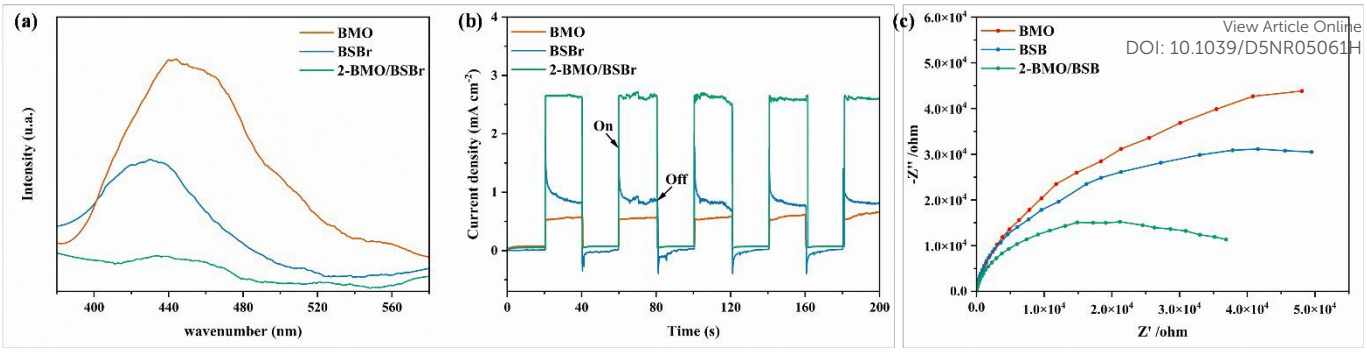

Figure 5. a) PL spectra, b) TPR, and c) EIS of BMO, BSBr, and 2-BMO/BSBr samples.

The photocatalytic CO2 reduction experiments of BMO, BSBr, and BMO/BSBr composite are carried out in water in the absence of sacrificial agent under visible light irradiation. As shown in Figure 6a, the measured CO production at hourly intervals over a five-hour duration exhibits approximately linear behavior, increasing with rising irradiation exposure time for all catalysts. After 5 h of light irradiation (Figure 6b), the CO production rates of the BMO and BSBr are only 7.57 and 1.75 μmol g^{-1} h^{-1}, respectively. In contrast, BMO/BSBr catalysts exhibit substantially higher CO yields compared to BMO and BSBr. Among them, 2-BMO/BSBr shows an optimal CO production rate of 34.4 μmol$g^{-1}h^{-1}$, representing 4.5-fold and 19.78-fold increase compared to the BMO and BSBr, respectively. Also, Figure S7 observed the photocatalytic CO evolution for the prepared samples using full spectrum irradiation. Moreover, the NMR analysis on the 2-BMO/BSBr sample (Figure S8) confirmed the absence of any liquid phase products. Furthermore, the 2-BMO/BSBr composite

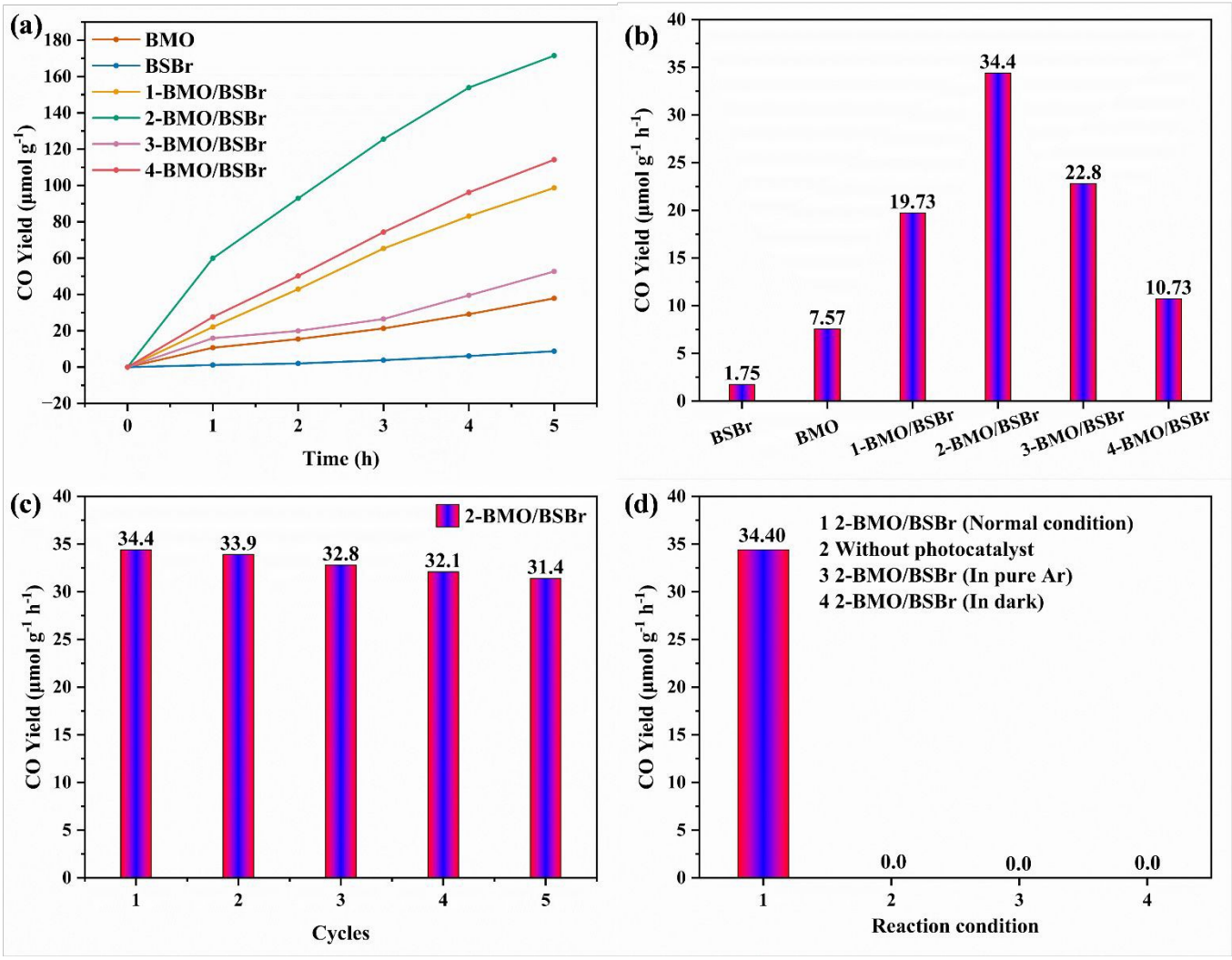

Figure 6. a and b) Photocatalytic CO evolution for the prepared samples. c) Stability of 2-BMO/BSBr sample. d) CO evolution rates under control conditions for 2-BMO/BSBr sample.

Open Access Article. Published on 02 March 2026. Downloaded on 3/3/2026 11:48:45 PM.
This article is licensed under a Creative Commons Attribution-NonCommercial 3.0 Unported Licence.

Nanoscale Accepted Manuscript

Please do not adjust margins

View Article Online
DOI: 10.1039/D5NR05064H

Open Access Article. Published on 02 March 2026. Downloaded on 3/3/2026 11:48:45 PM.
This article is licensed under a Creative Commons Attribution-NonCommercial 3.0 Unported Licence.

Nanoscale Accepted Manuscript

demonstrated high recyclability and durable stability, as evidenced by only a slight decrease in the CO yield rate over five consecutive photocatalytic cycles (Figure 6c). Subsequently, the catalyst is recovered and characterized after the cyclic experiments. A comparison of the XRD characterization results of the 2-BMO/BSBr sample before and after the cyclic experiments shows no significant changes (Figure S9), confirming that the fabricated photocatalyst not only possesses excellent catalytic stability but also remarkable structural and compositional integrity. Furthermore, three control experiments are conducted under specific conditions including a pure nitrogen atmosphere, the absence of light, and the absence of a photocatalyst. As shown in Figure 6d, the results reveal that no CO is formed under these conditions, confirming that the carbon source of CO is exclusively derived from CO_2. Furthermore, Isotope-labeled $^{13}CO_2$ was employed as the reaction gas source to determine whether CO production originated from the decomposition of CO_2. As shown in Figure S10, the isotopic experiment on the 2-BMO/BSBr photocatalyst after 5 h of illumination confirms that the predominant detected product was ^{13}CO (m/z = 29), unequivocally proving that the generated CO is exclusively derived from the photocatalytic CO_2 reduction.[91, 92]

2D/1D heterojunction mechanism

To explore the photocatalytic CO_2 conversion mechanism over the 2-BMO/BSBr, in situ diffuse reflectance infrared Fourier transform spectroscopy (DRIFTS) was performed. As shown in Figure 7a, the absorption band at approximately 1275 cm^{-1} can be attributed to bidentate carbonate (b-CO_3^{-2}),[93] while the absorbance peaks at 1437 cm^{-1} and 1672 cm^{-1} correspond to bicarbonate (HCO_3^{-1}).[93, 94] Additionally, the peak at 1552 cm^{-1} is indicative of the *COOH species.[95] The formation of *COOH is a critical intermediate step in the photocatalytic CO_2 reduction to CO.[96] Initially, CO_2 molecules are adsorbed onto the active sites of the 2-BMO/BSBr surface. Subsequently, the reaction processes involving H^+ and e^- facilitate the transformation of CO_2 into *COOH, which is further converted to CO. Finally, CO desorbs from the catalyst surface, completing the reaction cycle.

Moreover, for exploring the redox reaction mechanism and the active species during photocatalytic CO_2 reduction, electron paramagnetic resonance (EPR) measurements were carried out under light irradiation using a 300 W Xe lamp to identify the formation of superoxide radicals ($^{\bullet}O_2^-$) and hydroxyl radicals ($^{\bullet}OH$) over the BMO, BSBr, and 2-BMO/BSBr. In these measurements, 5,5-dimethyl-1-pyrroline-N-oxide (DMPO) was used as the spin-trapping reagent. As shown in Figure 7b, no diffraction peaks were observed in the dark for all the studied samples. The DMPO-$^{\bullet}O_2^-$ signals (1:1:1:1) for BMO and BSBr can be observed because their CB potential is more negative than that of $O_2/^{\bullet}O_2^-$ (0.33 V, pH = 7).[29, 67] Figure 7c shows the EPR spectra of DMPO-$^{\bullet}OH$ (1:2:2:1) for BMO, BSBr, and

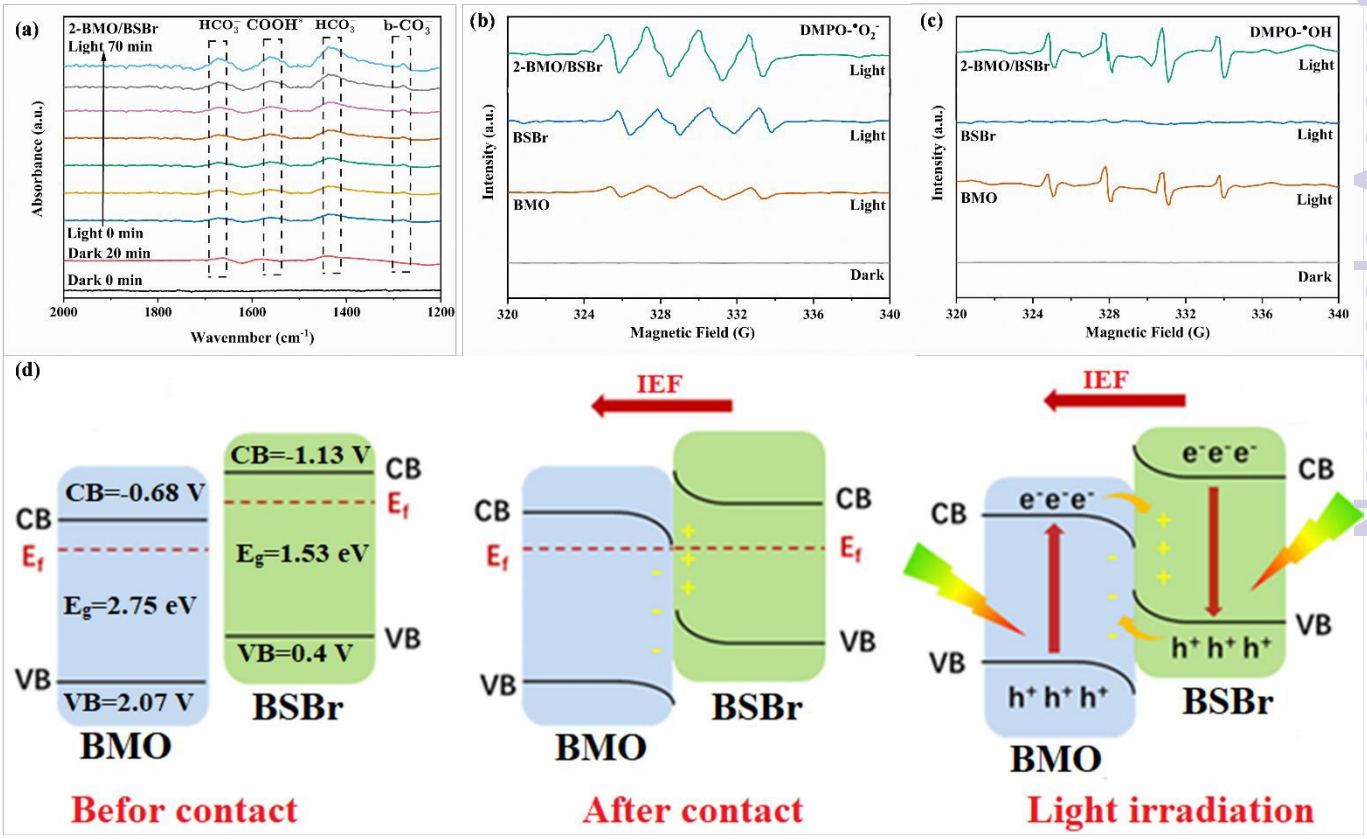

Figure 7. a) In-situ DRIFTS spectra of 2-BMO/BSBr composites. EPR spectra of b) DMPO-$^{\bullet}O_2^-$ and c) DMPO-$^{\bullet}OH$ of BMO, BSBr, 2-BMO/BSBr samples. d) Band structure for 2-BMO/BSBr.

Please do not adjust margins

View Article Online
DOI: 10.1039/D5NR05961H

2-BMO/BSBr.[76] Typically, BMO and 2-BMO/BSBr show significant DMPO-•OH signals, while BSBr shows negligible signal. This is because the potential of H_2O/•OH (1.90 V, pH = 7) is more positive than the VB potential of BSBr, resulting in the difficulty for BSBr to oxidize H_2O or OH^- to •OH.[28, 71]

By combining the results of DMPO-EPR radical trapping results with XPS evidence for the formation of strong interfacial chemical interactions and built in IEF, it can be concluded that the photogenerated electrons and holes are predominantly accumulated on the BSBr and BMO components of the 2-BMO/BSBr composite, respectively. This spatial charge distribution is characteristic of a direct Z-scheme heterojunction, as illustrated in Figure 7d, rather than a conventional type-II charge transfer pathway. Upon light irradiation (Figure 7d), electrons in both semiconductors are excited from the VB to the CB. Subsequently, the photoinduced electrons in the CB of BMO spontaneously migrate toward and recombine with the holes in the VB of BSBr, following the established Z-scheme mechanism.[33-36]

Conclusions

In summary, we have successfully fabricated a direct Z-scheme BMO/BSBr heterojunction photocatalyst incorporating built-in IEF and interfacial bonds interaction, which drastically enhance photocatalytic CO_2 reduction performance. Specifically, the formation of the direct Z-scheme heterojunction can significantly enhance the photogenerated charge carrier separation efficiency and redox capability of the BMO/BSBr. Under visible-light irradiation, the optimized 2-BMO/BSBr exhibits an outstanding photocatalytic CO production rate of 34.3 μmol g^{-1} h^{-1}, outperforming pristine BMO and BSBr by 4.5 and 19.7 times, respectively. Moreover, the BMO/BSBr demonstrates exceptional stability, maintaining >90% of its initial activity after cyclic tests. These findings provide a foundation for developing advanced heterojunction materials with atomic-level interfacial engineering for sustainable solar energy conversion applications.

Author contributions

We strongly encourage authors to include author contributions and recommend using CRediT for standardised contribution descriptions. Please refer to our general author guidelines for more information about authorship.

Conflicts of interest

In accordance with our policy on Conflicts of interest please ensure that a conflicts of interest statement is included in your manuscript here. Please note that this statement is required for all submitted manuscripts. If no conflicts exist, please state that "There are no conflicts to declare".

Data availability

A data availability statement (DAS) is required to be submitted alongside all articles. Please read our full guidance on data availability statements for more details and examples of suitable statements you can use.

Acknowledgements

This work was financially supported in part by the NSFC (52261135635, U23A2091).

References

1. D. Lee, X. Gao, L. Sun, Y. Jee, J. Poplawsky, T. O. Farmer, L. Fan, E.-J. Guo, Q. Lu and W. T. Heller, *Nature communications*, 2020, **11**, 1371.
2. J. Li, L. Cai, J. Shang, Y. Yu and L. Zhang, *Advanced materials*, 2016, **28**, 4059-4064.
3. H. Shang, X. Zhou, J. Dong, A. Li, X. Zhao, Q. Liu, Y. Lin, J. Pei, Z. Li and Z. Jiang, *Nature communications*, 2020, **11**, 3049.
4. H. Yu, F. Chen, X. Li, H. Huang, Q. Zhang, S. Su, K. Wang, E. Mao, B. Mei and G. Mul, *Nature communications*, 2021, **12**, 4594.
5. H. Yu, J. Li, Y. Zhang, S. Yang, K. Han, F. Dong, T. Ma and H. Huang, *Angewandte Chemie International Edition*, 2019, **58**, 3880-3884.
6. G. Zhang, Z. Hu, M. Sun, Y. Liu, L. Liu, H. Liu, C. P. Huang, J. Qu and J. Li, *Advanced Functional Materials*, 2015, **25**, 3726-3734.
7. K. Zhao, X. Nie, H. Wang, S. Chen, X. Quan, H. Yu, W. Choi, G. Zhang, B. Kim and J. G. Chen, *Nature communications*, 2020, **11**, 2455.
8. R. Bhosale, S. Jain, C. P. Vinod, S. Kumar and S. Ogale, *ACS Applied Materials & Interfaces*, 2019, **11**, 6174-6183.
9. F. Chen, H. Huang, L. Ye, T. Zhang, Y. Zhang, X. Han and T. Ma, *Advanced Functional Materials*, 2018, **28**, 1804284.
10. J. Di, X. Zhao, C. Lian, M. Ji, J. Xia, J. Xiong, W. Zhou, X. Cao, Y. She and H. Liu, *Nano Energy*, 2019, **61**, 54-59.
11. M. Gao, J. Yang, T. Sun, Z. Zhang, D. Zhang, H. Huang, H. Lin, Y. Fang and X. Wang, *Applied Catalysis B: Environmental*, 2019, **243**, 734-740.
12. D. Wu, L. Ye, H. Y. Yip and P. K. Wong, *Catalysis Science & Technology*, 2017, **7**, 265-271.
13. M. Wang, M. Shen, X. Jin, J. Tian, M. Li, Y. Zhou, L. Zhang, Y. Li and J. Shi, *ACS Catalysis*, 2019, **9**, 4573-4581.
14. Y. Wang, J. Hu, T. Ge, F. Chen, Y. Lu, R. Chen, H. Zhang, B. Ye, S. Wang and Y. Zhang, *Advanced Materials*, 2023, **35**, 2302538.
15. Z. Sun, X. Yang, X.-F. Yu, L. Xia, Y. Peng, Z. Li, Y. Zhang, J. Cheng, K. Zhang and J. Yu, *Applied Catalysis B: Environmental*, 2021, **285**, 119790.
16. Y. Zhou, Y. Zhang, M. Lin, J. Long, Z. Zhang, H. Lin, J. C. S. Wu and X. Wang, *Nature communications*, 2015, **6**, 8340.
17. S. Fang, M. Rahaman, J. Bharti, E. Reisner, M. Robert, G. A. Ozin and Y. H. Hu, *Nature Reviews Methods Primers*, 2023, **3**, 61.
18. H. Zhou, D. Zhang, H. Xie, Y. Liu, C. Meng, P. Zhang, F. Fan, R. Li and C. Li, *Advanced Materials*, 2023, **35**, 2300914.

Open Access Article. Published on 02 March 2026. Downloaded on 3/3/2026 11:48:45 PM.
This article is licensed under a Creative Commons Attribution-NonCommercial 3.0 Unported Licence.
Nanoscale Accepted Manuscript

Please do not adjust margins

Open Access Article. Published on 02 March 2026. Downloaded on 3/3/2026 11:48:45 PM.
This article is licensed under a Creative Commons Attribution-NonCommercial 3.0 Unported Licence.

View Article Online
DOI: 10.1039/D6NR00061F

19. J. Wu, X. Li, W. Shi, P. Ling, Y. Sun, X. Jiao, S. Gao, L. Liang, J. Xu and W. Yan, *Angewandte Chemie*, 2018, **130**, 8855-8859.
20. A. Kumar and V. Krishnan, *Advanced Functional Materials*, 2021, **31**, 2009807.
21. F. Chen, T. Ma, T. Zhang, Y. Zhang and H. Huang, *Advanced Materials*, 2021, **33**, 2005256.
22. X. Feng, R. Zheng, C. Gao, W. Wei, J. Peng, R. Wang, S. Yang, W. Zou, X. Wu and Y. Ji, *Nature Communications*, 2022, **13**, 2146.
23. Y. Shi, G. Zhan, H. Li, X. Wang, X. Liu, L. Shi, K. Wei, C. Ling, Z. Li and H. Wang, *Advanced Materials*, 2021, **33**, 2100143.
24. J. Liang, H. Zhang, Q. Song, Z. Liu, J. Xia, B. Yan, X. Meng, Z. Jiang, X. W. Lou and C. S. Lee, *Advanced Materials*, 2024, **36**, 2303287.
25. Z. Zhang, J. Huang, M. Zhang, Q. Yuan and B. Dong, *Applied Catalysis B: Environmental*, 2015, **163**, 298-305.
26. N. Li, X. Chen, J. Wang, X. Liang, L. Ma, X. Jing, D.-L. Chen and Z. Li, *ACS nano*, 2022, **16**, 3332-3340.
27. J. Fu, Q. Xu, J. Low, C. Jiang and J. Yu, *Applied Catalysis B: Environmental*, 2019, **243**, 556-565.
28. Z. Wang, B. Cheng, L. Zhang, J. Yu and H. Tan, *Solar RRL*, 2022, **6**, 2100587.
29. J. Wang, Y. Yu, J. Cui, X. Li, Y. Zhang, C. Wang, X. Yu and J. Ye, *Applied Catalysis B: Environmental*, 2022, **301**, 120814.
30. L. Zhang, J. Zhang, J. Yu and H. García, *Nature Reviews Chemistry*, 2025, 1-15.
31. M. Sayed, K. Qi, X. Wu, L. Zhang, H. García and J. Yu, *Chemical Society Reviews*, 2025, **54**, 4874-4921.
32. X. Wu, M. Sayed, G. Wang, W. Yu and B. Zhu, *Advanced Materials*, 2025, e11322.
33. F.-J. Zhang, Z.-C. Wang, Y.-H. Niu and J. Ma, *Solid State Sciences*, 2025, 108139.
34. J. Lian, D. Li, Y. Ma, H. Bian, Y. Shao, Z. Wang, J. Yan, R. Jiang, S. F. Liu and F. Zhang, *Chinese Chemical Letters*, 2025, 111394.
35. Y.-D. Feng, Y. Zhang, D.-D. Cheng, Y.-Y. Jia, H.-R. Zhu and L. Duan, *Molecular Catalysis*, 2025, **585**, 115368.
36. L. Zhang, X. Yin, X. Liu, W. Zhang, Y. Tian, X. Li, B. Li and S. Su, *Journal of Photochemistry and Photobiology A: Chemistry*, 2025, **460**, 116122.
37. L. Zhang, J. Zhang, H. Yu and J. Yu, *Advanced materials*, 2022, **34**, 2107668.
38. F. Xu, K. Meng, B. Zhu, H. Liu, J. Xu and J. Yu, *Advanced Functional Materials*, 2019, **29**, 1904256.
39. Z. Liu, X. Chang, Y. Shi and X. Zhao, *Journal of Alloys and Compounds*, 2025, **1010**, 177572.
40. Y. Huo, X. Zhou, F. Zhao, C. Ai, Z. Wu, Z. Chang and B. Zhu, *Acta Physico-Chimica Sinica*, 2025, 100148.
41. S. Wu, M. Xu, L. Ai, Q. Ma, C. Leng, N. Guo, H. Fan and L. Wang, *Journal of Colloid and Interface Science*, 2025, 138807.
42. J. Lee, G. I. Waterhouse, Y. Mao, Z. Wang, E. Zhu, J. Low, S.-P. Chai and L.-L. Tan, *Applied Catalysis B: Environment and Energy*, 2025, **365**, 124942.
43. H. Yang, Z. Wang, J. Zhang, K. Dai and J. Low, *Journal of Materiomics*, 2025, **11**, 100996.
44. Z. Xing, J. Hu, M. Ma, H. Lin, Y. An, Z. Liu, Y. Zhang, J. Li and S. Yang, *Journal of the American Chemical Society*, 2019, **141**, 19715-19727.
45. J. Li, G. Zhan, Y. Yu and L. Zhang, *Nature communications*, 2016, **7**, 11480.
46. Z.-K. Shen, M. Cheng, Y.-J. Yuan, L. Pei, J. Zhong, J. Guan, X. Li, Z.-J. Li, L. Bao and X. Zhang, *Applied Catalysis B: Environmental*, 2021, **295**, 120274.
47. Y. Zhang, Y. Huang, S. S. Zhu, Y. Y. Liu, X. Zhang, J. J. Wang and A. Braun, *Small*, 2021, **17**, 2100320.
48. Y. Ao, J. Xu, P. Wang, C. Wang, J. Hou, J. Qian and Y. Li, *Colloids and Surfaces A: Physicochemical and Engineering Aspects*, 2015, **487**, 66-74.
49. S. Salehian, A. Larimi, A. A. Asgharinezhad, N. Khallaghi, T. N. Borhani and C. Ghotbi, *Surfaces and Interfaces*, 2023, **42**, 103432.
50. Z. Liu, Y. Song, Q. Wang, Y. Jia, X. Tan, X. Du and S. Gao, *Journal of colloid and interface science*, 2019, **556**, 92-101.
51. J. Chi, Z. Jiang, J. Yan, A. Larimi, Z. Wang, L. Wang and W. Shangguan, *Materials Today Chemistry*, 2022, **26**, 101060.
52. M. Mehta, S. Krishnamurthy, S. Basu, T. P. Nixon and A. P. Singh, *Materials today chemistry*, 2020, **17**, 100283.
53. H. S. M. Abd-Rabboh, M. Benaissa, M. S. Hamdy, M. A. Ahmed and M. Glal, *Optical Materials*, 2021, **114**, 110761.
54. H. Li, L. Liang, X. Niu, D. Zhang, H. Fan and K. Wang, *New Journal of Chemistry*, 2022, **46**, 8185-8194.
55. X. Song, R. Wang, J. Wang, Z. Huang, S. Ye and D. D. Dionysiou, *Optical Materials*, 2021, **113**, 110839.
56. M. Ahmadi, S. M. Alavi and A. Larimi, *Catalysis Communications*, 2023, **179**, 106681.
57. Q. Wang, K. Wang, L. Zhang, H. Wang and W. Wang, *Applied Surface Science*, 2019, **470**, 832-839.
58. L. Cheng, L. Liu, D. Wang, F. Yang and J. Ye, *Journal of CO2 Utilization*, 2019, **29**, 196-204.
59. L. Liu, K. Dai, J. Zhang and L. Li, *Journal of Colloid and Interface Science*, 2021, **604**, 844-855.
60. Y. Dong, S. Dong, B. Liu, C. Yu, J. Liu, D. Yang, P. Yang and J. Lin, *Advanced Materials*, 2021, **33**, 2106838.
61. L. Zhang, T. Xu, X. Zhao and Y. Zhu, *Applied Catalysis B: Environmental*, 2010, **98**, 138-146.
62. N. Li, L. Zhu, W.-D. Zhang, Y.-X. Yu, W.-H. Zhang and M.-F. Hou, *Journal of alloys and compounds*, 2011, **509**, 9770-9775.
63. X. Zhang, G. Ren, C. Zhang, R. Li, Q. Zhao and C. Fan, *Catalysis Letters*, 2020, **150**, 2510-2516.
64. F. Deng, F. Zhong, L. Zhao, X. Luo, S. Luo and D. D. Dionysiou, *Journal of hazardous materials*, 2017, **340**, 85-95.
65. L. Ai, L. Wang, M. Xu, S. Zhang, N. Guo, D. Jia and L. Jia, *Applied Catalysis B: Environmental*, 2021, **284**, 119730.
66. Y. Chen, G. Tian, T. Feng, W. Zhou, Z. Ren, T. Han, Y. Xiao and H. Fu, *CrystEngComm*, 2015, **17**, 6120-6126.
67. J. Zhao, M. Ji, H. Chen, Y.-X. Weng, J. Zhong, Y. Li, S. Wang, Z. Chen, J. Xia and H. Li, *Applied Catalysis B: Environment and Energy*, 2022, **307**, 121162.
68. J. Li, W. Pan, Q. Liu, Z. Chen, Z. Chen, X. Feng and H. Chen, *Journal of the American Chemical Society*, 2021, **143**, 6551-6559.
69. W. Jia, R. Xiong, Y. Sun, Y. Xiao, B. Cheng and S. Lei, *Journal of Materials Chemistry A*, 2024, **12**, 4513-4524.
70. R. Niu, Q. Liu, B. Huang, Z. Liu, W. Zhang, Z. Peng, Z. Wang, Y. Yang, Z. Gu and J. Li, *Applied Catalysis B: Environmental*, 2022, **317**, 121727.
71. X. Li, J. Zhang, Z. Wang, J. Fu, S. Li, K. Dai and M. Liu, *Chemistry–A European Journal*, 2023, **29**, e202202669.
72. X. Wu, Q. Zhang and C. Su, *FlatChem*, 2021, **27**, 100244.

Nanoscale Accepted Manuscript

Please do not adjust margins

View Article Online
DOI: 10.1039/D5NR05061H

Open Access Article. Published on 02 March 2026. Downloaded on 3/3/2026 11:48:45 PM.
This article is licensed under a Creative Commons Attribution-NonCommercial 3.0 Unported Licence.

Nanoscale Accepted Manuscript

73. Z. Zhang, T. Zheng, J. Xu and H. Zeng, *Journal of materials science*, 2016, **51**, 3846-3853.
74. A. Phuruangrat, P. Jitrou, P. Dumrongrojthanath, N. Ekthammathat, B. Kuntalue, S. Thongtem and T. Thongtem, *Journal*, 2013.
75. J. He, J. Lin, Y. Zhang, Y. Hu, Q. Huang, G. Zhou, W. Li, J. Hu, N. Hu and Z. Yang, *Chemical Engineering Journal*, 2024, **480**, 148036.
76. J. Zhang, M. Zheng, Y. Wu, J. Xiong, S. Li, W. Jiang, Z. Liu and J. Di, *ACS Nano*, 2025, **19**, 2759-2768.
77. X. Xie, Q.-U. Hassan, H. Lu, F. Rao, J. Gao and G. Zhu, *Chinese Chemical Letters*, 2021, **32**, 2038-2042.
78. X. Li, W. Zhang, J. Li, G. Jiang, Y. Zhou, S. Lee and F. Dong, *Applied Catalysis B: Environmental*, 2019, **241**, 187-195.
79. W. C. Huo, J. Y. Li, M. Liu, X. Y. Liu, Y. X. Zhang and F. Dong, *Chemical Engineering Journal*, 2019, **361**, 129-138.
80. E. A. Abdullah, A. H. Abdullah, Z. Zainal, M. Z. Hussein and T. K. Ban, *Journal of Chemistry*, 2012, **9**, 2429-2438.
81. S. M. Ramay, H. Kassim, A. Mahmood, A. A. Siddig and N. S. Al Zayed, *Journal of Materials Science: Materials in Electronics*, 2022, **33**, 14343-14355.
82. R. K. Chava, Y. Im and M. Kang, *Journal of Materials Chemistry A*, 2024, **12**, 18498-18511.
83. M. Jin, S. Lu, L. Ma and M. Gan, *Applied Surface Science*, 2017, **396**, 438-443.
84. Z. Cai, Y. Huang, H. Ji, W. Liu, J. Fu and X. Sun, *Separation and Purification Technology*, 2022, **280**, 119772.
85. C. Li, S. Gu, Y. Xiao, X. Lin, X. Lin, X. Zhao, J. Nan and X. Xiao, *Journal of Colloid and Interface Science*, 2024, **668**, 426-436.
86. S. Maswanganyi, R. Gusain, N. Kumar, E. Fosso-Kankeu, F. B. Waanders and S. S. Ray, *ACS omega*, 2021, **6**, 16783-16794 .
87. J. Zhao, Q. Lu, M. Wei and C. Wang, *Journal of Alloys and Compounds*, 2015, **646**, 417-424.
88. B. Huang, X. Fu, K. Wang, L. Wang, H. Zhang, Z. Liu, B. Liu and J. Li, *Advanced Powder Materials*, 2024, **3**, 100140.
89. R. Yuan, C. Yue, J. Qiu, F. Liu and A. Li, *Applied Catalysis B: Environmental*, 2019, **251**, 229-239.
90. X. Gao, G. Tang, W. Peng, Q. Guo and Y. Luo, *Chemical Engineering Journal*, 2019, **360**, 1320-1329.
91. S. Wang, X. Hai, X. Ding, S. Jin, Y. Xiang, P. Wang, B. Jiang, F. Ichihara, M. Oshikiri and X. Meng, *Nature communications*, 2020, **11**, 1149.
92. Z. K. Xin, Y. J. Gao, Y. Gao, H. W. Song, J. Zhao, F. Fan, A. D. Xia, X. B. Li, C. H. Tung and L. Z. Wu, *Advanced Materials*, 2022, **34**, 2106662.
93. B. Wang, J. Di, L. Lu, S. Yan, G. Liu, Y. Ye, H. Li, W. Zhu, H. Li and J. Xia, *Applied Catalysis B: Environmental*, 2019, **254**, 551-559.
94. X. Li, L. Liang, Y. Sun, J. Xu, X. Jiao, X. Xu, H. Ju, Y. Pan, J. Zhu and Y. Xie, *Journal of the American Chemical Society*, 2018, **141**, 423-430.
95. X. Li, Y. Sun, J. Xu, Y. Shao, J. Wu, X. Xu, Y. Pan, H. Ju, J. Zhu and Y. Xie, *Nature Energy*, 2019, **4**, 690-699.
96. J. Di, C. Chen, S.-Z. Yang, S. Chen, M. Duan, J. Xiong, C. Zhu, R. Long, W. Hao and Z. Chi, *Nature communications*, 2019, **10**, 2840.

Please do not adjust margins

View Article Online
DOI: 10.1039/D5NR05061H

Data Availability

All data needed to evaluate the conclusions in the paper are present in the paper and the Supplementary Information. Additional data related to this paper may be requested from the authors.

Open Access Article. Published on 02 March 2026. Downloaded on 3/3/2026 11:48:45 PM.
This article is licensed under a Creative Commons Attribution-NonCommercial 3.0 Unported Licence.

Nanoscale Accepted Manuscript